



UNIVERSITY OF LEEDS

This is a repository copy of *Microbubble coalescence and breakup in turbulent vertical channel flows*.

White Rose Research Online URL for this paper:
<http://eprints.whiterose.ac.uk/134970/>

Version: Accepted Version

Proceedings Paper:

Asiagbe, KS orcid.org/0000-0001-6957-8597, Fairweather, M, Njobuenwu, DO orcid.org/0000-0001-6606-1912 et al. (1 more author) (2019) Microbubble coalescence and breakup in turbulent vertical channel flows. In: Proceedings of the Ninth International Symposium on Turbulence, Heat and Mass Transfer. Turbulence, Heat and Mass Transfer 9, 10-13 Jul 2018, Rio de Janeiro, Brazil. Begell-House Inc , pp. 523-534. ISBN 978-1-56700-468-7

This is an author produced version of a conference paper published in Proceedings of the Ninth International Symposium On Turbulence, Heat and Mass Transfer. Uploaded in accordance with the publisher's self-archiving policy.

Reuse

Items deposited in White Rose Research Online are protected by copyright, with all rights reserved unless indicated otherwise. They may be downloaded and/or printed for private study, or other acts as permitted by national copyright laws. The publisher or other rights holders may allow further reproduction and re-use of the full text version. This is indicated by the licence information on the White Rose Research Online record for the item.

Takedown

If you consider content in White Rose Research Online to be in breach of UK law, please notify us by emailing eprints@whiterose.ac.uk including the URL of the record and the reason for the withdrawal request.



eprints@whiterose.ac.uk
<https://eprints.whiterose.ac.uk/>

Microbubble coalescence and breakup in turbulent vertical channel flows

K.S. Asiagbe, M. Fairweather, D.O. Njobuenwu and M. Colombo

School of Chemical and Process Engineering, University of Leeds, Leeds LS2 9JT, UK

pmksa@leeds.ac.uk, m.fairweather@leeds.ac.uk, d.o.njobuenwu@leeds.ac.uk,
m.colombo@leeds.ac.uk

Abstract – Large eddy simulation coupled to Lagrangian bubble tracking is used to study four-way coupled turbulent bubbly flow in channels, including bubble collision, coalescence and breakup. Upward and downward vertical channel flows of water at shear Reynolds numbers of 150 and 2000 are examined, with air bubbles of diameter $d_b = 220 \mu\text{m}$ dispersed within the flows. Additional simulations are performed for the case of refrigerant R134a at a shear Reynolds number of 1154. The ability of the model to predict coalescence and breakup is evaluated, as well as the impact of the flow condition on the two phenomena. Coalescence and breakup are favoured in upflow conditions, with turbulence found to significantly impact the level of bubble interaction. Coalescence is dominant at low turbulence levels and breakup, which was only detected in the R134a flow, is favoured at high turbulence. The results demonstrate the capabilities of the overall model to predict bubble coalescence and breakup, and its usefulness for predicting flows that are of industrial relevance where interfacial area and bubble size distribution govern interfacial mass, momentum and heat transfer processes.

1. Introduction

The relevance of bubbly flows extends over many industrial sectors, such as the chemical and process industries, nuclear energy, oil and gas extraction and treatment, and bioenergy, as well as being of significance in medical and pharmaceutical applications. In these flows, interfacial transfer processes, and their impact on mixing and heat and mass transfer in the flow, are of particular interest. These processes are mainly governed by the interfacial area and the topology of the interface between phases that evolves continuously with the bubble size distribution in the flow. In turbulent flows, most of the latter changes result from bubble coalescence and breakup events induced by interactions between the bubbles and the turbulence field. At the present time, however, knowledge of these processes is limited, and there is no general agreement on a commonly accepted formulation for their prediction.

Bubbly flows are characterized by many physical complexities for which a complete understanding is still missing and difficult to achieve. In such flows, many complicated inter-relations and feedbacks exist among the mechanisms governing phase distribution, the relative motion between the phases, interfacial transfer processes, and coalescence and breakup events. These govern changes in the bubble size distribution and strongly depend on the continuous phase turbulence field. Although challenging, achieving a better understanding of these complex phenomena is of utmost importance in obtaining correct and physically based predictions of bubbly flows, and in allowing more reliable predictions of their behaviour.

Four-way coupled simulations, accounting for interaction and collision in the

dispersed phase field, have been addressed with Eulerian-Lagrangian techniques, but mainly for multiphase solid particle flows [1-5]. More recent and limited have been applications to dispersed bubbly flows [6-8]. These have been most often addressed using averaged Eulerian-Eulerian multi-fluid models, where evolution of the average bubble size distribution is predicted using population balance models. A number of these models were assessed in the work of Deju et al. [9], namely the direct quadrature method of moments, the average bubble number density model and the homogeneous multi-size-group model. Their ability to track changes in the gas void fraction and bubble size distribution under complex flow conditions were evaluated and model predictions validated against experimental measurements in medium-sized and large vertical pipes under different gas injection methods and flow conditions. The bubble size evolution was found to exhibit a coalescence dominated trend in the medium-sized pipe. In contrast, bubble break-up was found to be dominant in large pipes. It is worth noting that the majority of studies performed to date have also investigated coalescence and breakup in turbulent flows for bubbles of diameters in the range 1-4 mm [10-12]. Smaller bubbles (fractions of mm in diameter) have been rarely addressed. Such small bubble sizes, as well as having dimensions that fit well with the point-particle hypothesis of Eulerian-Lagrangian treatments, are highly relevant in drag reduction, enhanced oil recovery and waste management applications, as well as in nuclear reactor core cooling (at high pressure).

Prediction of population balance approaches and the accuracy of coalescence and breakup models strongly depends on turbulence in the continuous field and the turbulence modelling approach used to predict it [9]. In previous studies, turbulence modulation in bubbly flows due to the dispersed bubbles has been widely discussed and analysed by comparing turbulence statistics for different bubble sizes and properties [13-15]. However, detailed analysis of the impact of turbulence on four-way coupled simulations and predictions of the models used to account for bubble coalescence and breakup have rarely been performed.

In this work, the main aim is to develop a computational model able to address, predict with accuracy, the dynamics of coalescence and breakup processes in turbulent bubbly flows, and the mutual interactions between these processes and the turbulence field. In order to do this, bubble collision, coalescence and breakup models are introduced into a Lagrangian bubble tracking routine previously developed to study bubbly flows in channels [16]. The Lagrangian tracker is implemented in a large eddy simulation (LES) capable of accurately predicting the continuous phase turbulent flow field. The deterministic bubble collision model assumes binary collisions using a hard-sphere approach [5]. Coalescence is modelled with the film drainage method of Prince and Blanch [17] and breakup with the model of Martinez-Bazan et al. [18]. The overall model is applied to vertical upward and downward channel flows of air bubbles in water at shear Reynolds numbers $Re_\tau = 150$ and 2000. An additional simulation for the turbulent flow of refrigerant R134a at an equivalent shear Reynolds number of $Re_\tau = 1154$, which became necessary to study the behaviour of the breakup model, is also reported.

2. Numerical Model

In LES, the Navier-Stokes equations are filtered and the flow field is decomposed such that the large scale motions are resolved in the computation, while the small sub-grid scale (SGS) motions are modelled. The flow field is obtained from solution of

the filtered forms of the mass and momentum balance equations:

$$\frac{\partial \bar{\rho}}{\partial t} + \frac{\partial \bar{\rho} \bar{u}_i}{\partial x_i} = 0 \quad (1)$$

$$\frac{\partial \bar{u}_i}{\partial t} + \frac{\partial (\bar{u}_i \bar{u}_j)}{\partial x_j} = -\frac{1}{\rho} \frac{\partial \bar{p}}{\partial x_i} + \frac{\partial}{\partial x_j} \left[\nu \left(\frac{\partial u_j}{\partial x_i} + \frac{\partial u_i}{\partial x_j} \right) - \tau_{ij}^{sgs} \right] + \bar{S}_{mom,i} \quad (2)$$

Here, ρ is the density and S_{mom} is a momentum source term which includes the pressure gradient that drives the flow and the feedback effects on the fluid from the dispersed phase. To close the above set of equations, modelling is required for the sub-grid scale stress tensor, τ_{ij}^{sgs} , which arises from top-hat filtering of the instantaneous Navier-Stokes equations. Reducing the filter width causes the majority of the energy spectrum to be resolved and, when the filter width tends to zero, the LES solution approaches the direct numerical simulation (DNS) limit [19]. The sub-grid stresses were modelled using the dynamic approach of Germano et al. [20], applied using the approximate localization procedure of Piomelli and Liu [21] and the modifications proposed by Di Mare and Jones [22]. In the model, the sub-grid stresses are calculated from the SGS eddy kinematic viscosity, ν_{SGS} , and the filtered part of the strain tensor $\bar{S}_{ij} = 0.5(\partial \bar{u}_i / \partial x_j + \partial \bar{u}_j / \partial x_i)$. The SGS viscosity is the product of the filter length Δ and an appropriate velocity scale taken to be $\Delta \|\bar{S}_{ij}\|$, hence $\nu_{sgs} = (C_s \Delta^2) \|\bar{S}_{ij}\|$. Therefore, the anisotropic part of the SGS stresses is:

$$\tau_{ij}^{sgs} = 2C_s \Delta^2 \|\bar{S}_{ij}\| \bar{S}_{ij} \quad (3)$$

where C_s is the Smagorinsky constant. In the dynamic model, estimation of C_s is achieved by applying a second filtering operation to obtain the test-filtered SGS stresses $T_{ij} = \overline{\bar{u}_i \bar{u}_j} - \bar{u}_i \bar{u}_j$. Here, the topmost overbar represents the test filter operation. The parameter T_{ij} is related to the SGS stress tensor $\bar{\tau}_{ij}$ by Germano's identity [23] through the resolved stress tensor $L_{ij} = T_{ij} - \bar{\tau}_{ij}$, which can be calculated from the resolved quantities. To obtain the required expression for the grid-filter level constant C_s , a relationship with the test-filter level constant values $C_s^2(\bar{\bullet})$ must be specified. Assuming that the cut-off length falls inside the inertial sub-range, $C^2 = C^2(\bar{\bullet})$. However, such a sub-range is not guaranteed to occur in wall bounded or low Reynolds number flows, with the largest deviation from universality of the SGS motions expected to occur in the regions of weakest resolved strain. Based on this, the two parameters at two different filter levels may differ. To account for this, Di Mare and Jones [22] proposed the following relation:

$$C_s^2(\bar{\bullet}) = C_s^2 \left(1 + \frac{\epsilon}{2\sqrt{2}\Delta^2 \|\bar{S}\| \|\bar{S}^a\|^2} \right) \quad (4)$$

where ϵ represents the turbulence energy dissipation rate, such that $\epsilon \sim v^3/l$, with $v = u_b$ and $l = h$ being a velocity and length scale, respectively (u_b and h are the bulk velocity and channel half-height for the flows considered herein).

As noted, Eq. **Error! Reference source not found.**) is related to the assumption

that the scale invariance of C_s can only be invoked if the cut-off falls inside the inertial sub-range and, when this occurs, the modelled dissipation represents the entire dissipation in the flow. Conversely, in the high Reynolds number limit, the dissipation is only determined by v and l so that the ratio of ϵ to $\bar{\Delta}^2 \|\bar{\mathbf{S}}\|^3$ is a measure of how far the flow is from scale preserving conditions. This equation represents a first-order expansion of other scale dependent expressions for C_s , e.g. that of Porté-Agel et al. [24], that also uses a single length and velocity scale. The main advantage of this method is that it is well-conditioned and avoids the spiky and irregular behaviour exhibited by some implementations of the dynamic model and, as the resolved strain tends to zero, C_s^2 also tends to zero, while $C_s^2(\bar{\bullet})$ remains bounded. The dissipation term also yields smooth C_s^2 fields without a need for averaging, and the maxima of C_s^2 are of the same order of magnitude as estimated by Lilly [25] for the Smagorinsky model constant. Negative values of the model parameters are not prevented, with such values set to zero to prevent instability. Negative values of the SGS viscosity are similarly set to zero. In this work, test filtering was performed in all space directions and no averaging of the calculated model parameter field was made. The ratio of the test to the grid filter ratio $\check{\Delta}/\Delta$ was set to 2.

Bubble motion in the turbulent flow field was obtained from Newton's second law of motion for each individual bubble [26]:

$$\frac{d\mathbf{v}}{dt} = \left(1 - \frac{\rho_l}{\rho_b}\right)g + \frac{\mathbf{u} - \mathbf{v}}{\tau_b} C_{SN} + C_L \frac{\rho_l}{\rho_b} [(\mathbf{u} - \mathbf{v}) \times \boldsymbol{\omega}] + \frac{\rho_l}{\rho_b} \frac{D\mathbf{u}}{Dt} + \frac{\rho_l}{2\rho_b} \left(\frac{D\mathbf{u}}{Dt} - \frac{d\mathbf{v}}{dt}\right) + \boldsymbol{\chi}_{sgs} \quad (5)$$

The terms on the right-hand side of Eq. (5) represent the different forces acting on a bubble, which are the gravity/buoyancy, drag, shear lift, pressure gradient and added mass forces, respectively. The final term, $\boldsymbol{\chi}_{sgs}$, represents the effect of SGS velocity fluctuations on the bubble motion and was determined using a stochastic Markov model [27]. The subscripts l and b indicate the liquid and bubble, respectively. τ_b is the bubble response time, expressed as $\tau_b = \rho_b d_b^2 / 18\mu$, with d_b the bubble diameter and μ the fluid dynamic viscosity. τ_b was additionally corrected to account for added mass effects, resulting in $\tilde{\tau}_b = \tau_b(1 + \rho/(2\rho_b)) \approx 358.6\tau_b$ [28]. C_{SN} and C_L represent the drag and lift coefficients. C_{SN} modifies the Stokesian drag force for large bubble Reynolds numbers [29] and is equal to $(1 + 0.15 \text{Re}_b^{0.687})$. The lift coefficient C_L is a function of the flow Reynolds number and was calculated using the model of Legendre and Magnaudet [30]. Perfectly elastic collisions were assumed at solid walls when the microbubble centre was located at a distance from the wall lower than the bubble radius [5].

Four-way coupled simulations were obtained by accounting for bubble-bubble collisions, bubble coalescence and breakup. Bubble collisions were assumed to be binary and modelled using a hard-sphere approach [5, 31]. Once a bubble-bubble collision was detected, the coalescence algorithm determined if the interaction resulted in a coalescence event. Coalescence was modelled following the film drainage theory proposed by Prince and Blanch [17]. The model assumes that a thin liquid film is trapped between the two colliding bubble. If the contact time is sufficient for this liquid film to drain away, the two bubbles coalesce, otherwise the bubbles bounce off without coalescence taking place. The contact time is expressed as $\tau_{ij} = (C_c R_{ij}) u_n^{-1}$, where R_{ij} is the equivalent bubble radius, given by $R_{ij} = 2.0(2/d_{b1} + 2/d_{b2})^{-1}$, and u_n is the relative approach velocity in the normal direction, with C_c the

deformation distance as a fraction of the effective bubble radius. The film drainage time is given by $t_{ij} = (R_{ij}^3 \rho_l / 16\sigma)^{0.5} \ln(h_0/h_f)$, with the initial film thickness h_0 set to 1.0×10^{-4} m and the final film thickness before rupture h_f set to 1.0×10^{-8} m, where σ is the surface tension. The properties of the new bubble after coalescence were calculated from a mass and momentum balance. Total bubble volume was conserved during the coalescence process and the bubble diameter after coalescence was obtained from $d_{b,new} = (d_{d1}^3 + d_{d2}^3)^{1/3}$.

As a consequence of the interaction with the turbulence field, bubbles can also breakup. In this work, the breakup of bubbles was modelled following the work of Martinez-Bazan et al. [18]. When bubbles are introduced into a turbulent fluid, the velocity fluctuations cause pressure deformation forces on the bubble surface and when these forces exceed the restoration effect due to the surface tension, the bubble breaks. Therefore, surface tension is one of the most important parameters in any breakup study. Surface tension arises from the difference between the intermolecular forces across an interface between two immiscible fluids. The resultant product is a force per unit length, or an energy per unit area, which resists the creation of a new interface [32]. The minimum energy required to deform a bubble of size d_b is therefore equal to its surface energy $E_s = \pi\sigma d_b^2$, which results in a surface restoring pressure $\tau_s = 6\sigma/d_b$. The pressure deformation force from the turbulence field is expressed as $\tau_t = \frac{1}{2}\rho_l\beta\epsilon^{2/3}d_b^{2/3}$, where $\beta = 8.2$.

Table 1: Computational parameters.

Re_τ	d_b (μm)	n_b (-)	σ (Nm^{-1})	ρ_b (kgm^{-3})	ϕ_v	t^+
150	220	226550	7.2×10^{-2}	1.3	10^{-3}	2000
2000	220	226550	7.2×10^{-2}	1.3	10^{-3}	2500
1154	220	226550	8.1×10^{-3}	28.4	10^{-3}	2500

The computational domain was a vertical channel having dimensions of $4\pi h \times 2\pi h \times 2h$ in the z (streamwise), y (spanwise) and x (wall-normal) directions, respectively (Fig. 1). The channel half-height h was equal to 0.02 m. Grid nodes were uniformly distributed along the y and z axes and non-uniformly in the wall-normal direction, giving a total of $128 \times 128 \times 129$ nodes. Periodic boundary conditions were imposed in the streamwise and spanwise directions, with no-slip conditions enforced at the channel walls for the liquid phase, and elastic collisions assumed for the bubbles.

Microbubbles of diameter $d_b = 220 \mu\text{m}$ were injected uniformly into fully-converged single-phase flow solutions. The bubble volume fraction was high enough for the microbubbles to affect the continuous phase flow field, as well as permitting significant bubble-bubble interaction. Air bubbles of density $\rho_b = 1.3 \text{ kgm}^{-3}$ were injected in the water flows at $Re_\tau = 150$ and 2000. In addition, bubbles of refrigerant R134a, having a density $\rho_b = 28.4 \text{ kgm}^{-3}$, were injected in a refrigerant flow of equivalent shear Reynolds number $Re_\tau = 1154$. R134a is a refrigerant commonly used in a wide range of refrigeration and air conditioning equipment [33]. The much lower surface tension ($\sigma = 0.0081 \text{ Nm}^{-1}$) with respect to the air-water mixture ($\sigma = 0.072 \text{ Nm}^{-1}$) promoted the

occurrence of breakup, and the refrigerant flow hence allowed a detailed study of this phenomenon. Computational parameters are summarized in Table 1.

The total simulation time is expressed in dimensionless units as $t^+ = tu_\tau^2/\nu$, where t is the computational time in seconds and u_τ^2 is the square of the shear velocity (defined as the square root of the ratio of shear at the wall, τ_w , to the fluid density). From the time at which the bubbles were first introduced, the simulation time t^+ was 2000 for the $Re_\tau = 150$ flow, and 2500 for the $Re_\tau = 2000$ case, with averaging carried out after 1000 t^+ . These values were found to be sufficient to ensure convergence of averaged quantities, and constant profiles of bubble concentration. Here, and below, the superscript (+) refers to a non-dimensional quantity scaled by the wall (viscous) variables, where u_τ/ν , u_τ and ν/u_τ^2 are the characteristic length, velocity and time scales.

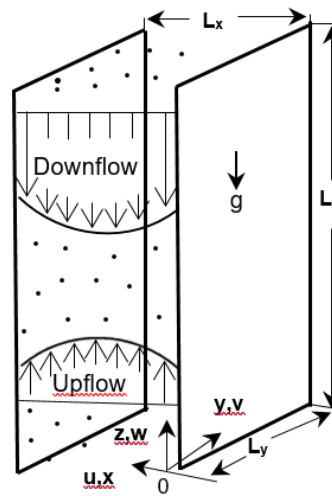


Figure 1: Computational domain and co-ordinate system for vertical channel flows.

3. Results and Discussion

Initially, and before injecting the bubbles, single-phase fluid simulations were run until they reached fully-developed conditions. Instantaneous two-dimensional snapshots of the streamwise velocity u_z are presented in Fig. 2 for the two shear Reynolds numbers $Re_\tau = 150$ and $Re_\tau = 2000$. Higher velocities and levels of turbulence are found in the higher Reynolds number flow, with turbulence dominating the overwhelming majority of the channel in this case, confining viscous effects and the viscous sublayer to the very near-wall regions.

Two-phase flow results with microbubbles are presented in Fig. 3, where the bubble streamwise mean velocity and the spatial distribution of coalescence events at $t^+ = 2000$ across the wall-normal direction are shown for $Re_\tau = 150$, for both upflow and downflow cases. A clear difference between the streamwise velocities in the two flow directions is apparent. Under the influence of buoyancy, lighter bubbles flow faster than the fluid in upflow and slower in downflow, and the relative velocity between the microbubbles and the fluid is the result of a balance between buoyancy and the interphase drag force. As a consequence, the drag force accelerates the liquid phase in upflow, increasing the mean streamwise velocity of the fluid. Conversely, bubbles decelerate the liquid phase in downflow, reducing the mean streamwise velocity of the fluid.

Significant differences are also shown in the coalescence distribution. A greater number of coalescence events was recorded in upflow, with these being concentrated in the near-wall regions. Similarly in downflow, the greatest number of coalescences, although lower than for the upflow case, was recorded in the near-wall regions. This is a consequence of the near-wall being the region of highest turbulence. Therefore, the probability of collision between bubbles and subsequent coalescence is greatest in this region. In channels and pipes, it is well known that bubbles, under the action of the lift force, migrate towards the wall in upflow, whereas they are prevented from reaching the near-wall region and preferentially concentrate in the centre of the flow in downflow. This difference in bubble concentration explains the higher number of coalescence events that were recorded in upflow, where the largest number of bubbles was found in the regions of highest turbulence. The number of coalescences is still the greatest near the wall in downflow, but the total number is significantly lower than in upflow because of the limited number of bubbles in these regions. This phenomenon is in show good agreement with the findings of previous DNS and experimental works [28, 34].

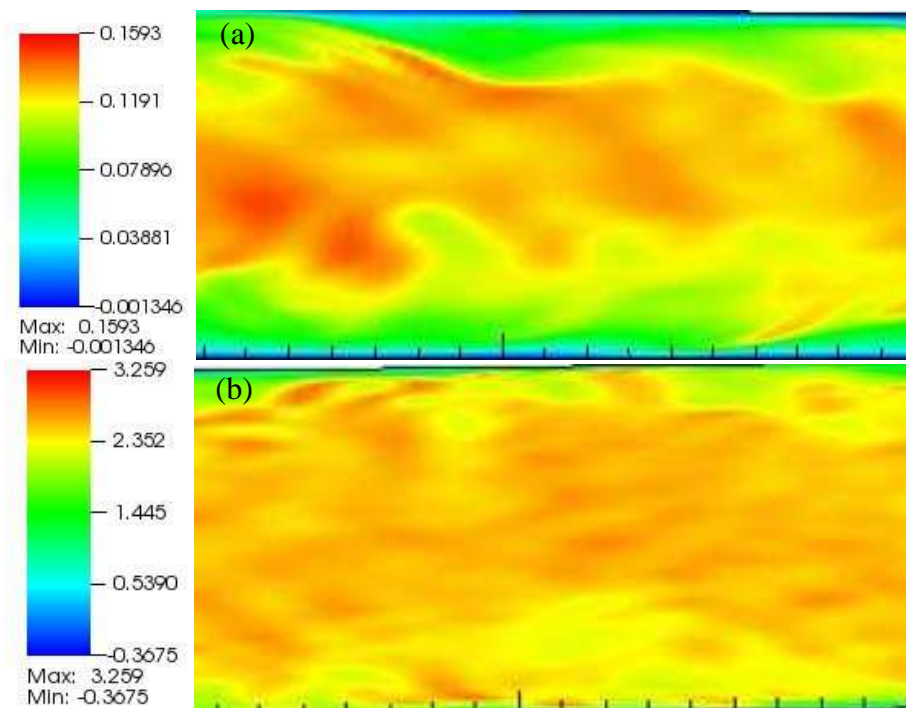


Figure 2: Two-dimensional representation of instantaneous velocity in the single phase turbulent flows for (a) $Re_\tau = 150$ and (b) $Re_\tau = 2000$.

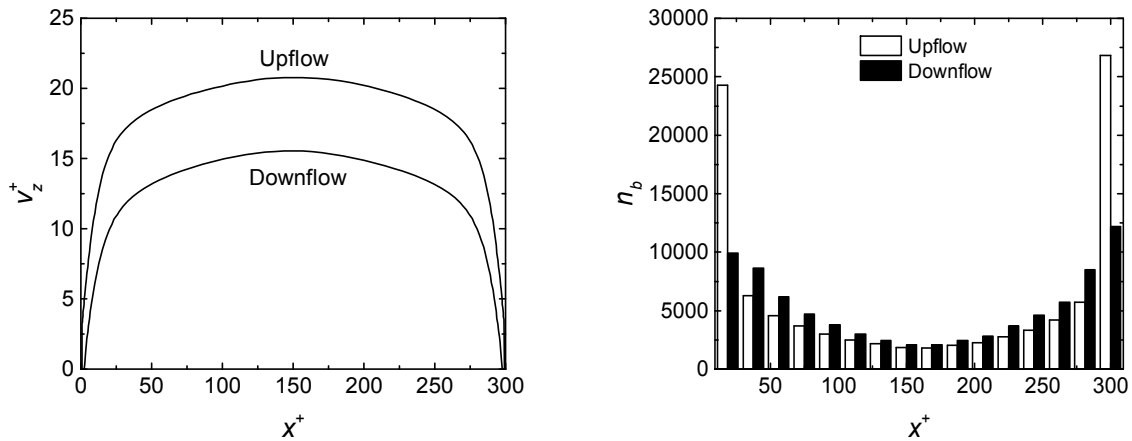


Figure 3: Bubble streamwise mean velocity (left) and number of bubble coalescences across channel width at $t^+ = 2000$ (right) in the $Re_\tau = 150$ flow.

No break-up was recorded in the $Re_\tau = 150$ flow, as a consequence of the turbulence level being insufficient to overcome the stabilizing effect of the surface tension. Therefore, simulations at the higher Reynolds number $Re_\tau = 2000$ were carried out and results are reported in Fig. 4, again for the streamwise mean velocity and coalescence distribution. Velocities are higher as a consequence of the higher Reynolds number. However, the relative velocity between the bubbles and the fluid remains almost constant, this being mainly a function of the constant bubble diameter. Therefore, differences between the bubbles' streamwise mean velocities in the two flow directions are much less evident in Fig. 4. The number of coalescence events is still greater for the upflow case, with higher levels of coalescence again occurring in the near-wall regions, although the differences between the two flow directions are much less pronounced than for the lower Reynolds number flow shown in Fig. 3 and, very close to the wall, the number of coalescences was actually reduced. The higher level of turbulence in this flow causes a decrease in the coalescence efficiency and, particularly in upflow, a much higher number of collision events that do not result in coalescence, in agreement with the film drainage theory. In addition, the higher turbulence level partially overrides the effect of the lift force and preferential bubble concentration was more limited at $Re_\tau = 2000$. Therefore, the coalescence event distribution is more uniform across the wall-normal direction for both flow directions.

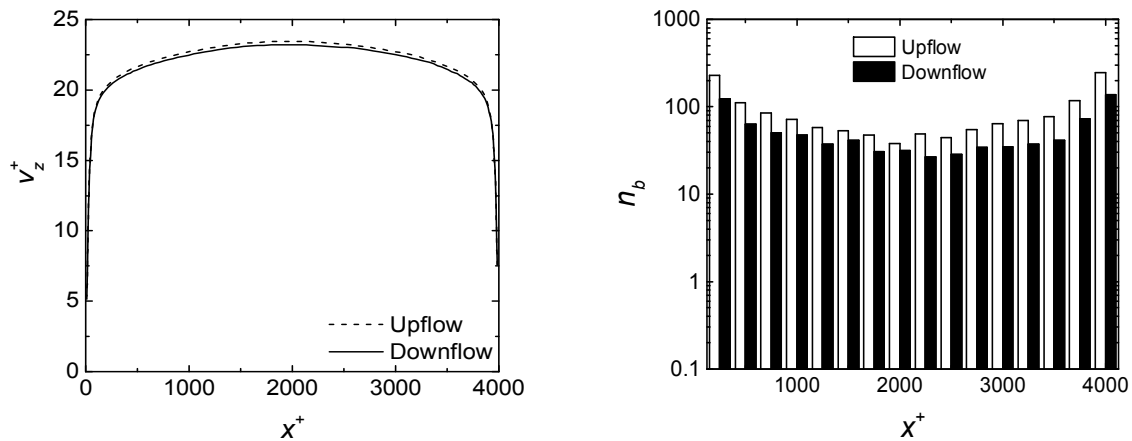


Figure 4: Bubble streamwise mean velocity (left) and number of bubble coalescences across channel width at $t^+ = 2000$ (right) in the $Re_\tau = 2000$ flow.

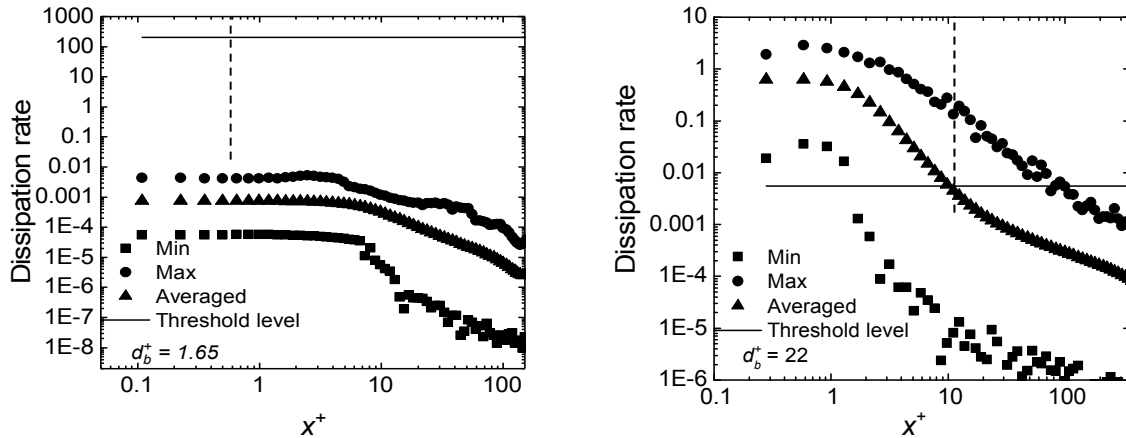


Figure 5: Required levels of turbulence energy dissipation rate to break spherical bubbles of $220 \mu\text{m}$ (1.65 wall units) diameter (threshold value) together with minimum, maximum and average levels of dissipation rate across channel flow in wall units for $Re_\tau = 150$ flow (left) and $Re_\tau = 1154$ refrigerant flow (right). Dashed vertical line indicates radius of bubble in contact with wall.

Despite the higher turbulence levels, no significant break-up was recorded even at $Re_\tau = 2000$, with the surface tension of the air-water mixture still high enough to counteract any inertia-driven surface deformation. Therefore, in order to allow the study of bubble breakup, additional simulations were carried out using refrigerant R134a at an equivalent shear Reynolds number $Re_\tau = 1154$. R134a bubbles were injected into the fully-developed single-phase refrigerant flow, assuming the mixture to be under saturation conditions (although heat transfer is neglected in this work). Refrigerant R134a has a much lower surface tension than for an air-water mixture (Table 1), and the impact of this is considered in more detail in Fig. 5. This figure gives predicted minimum, maximum and average values of the turbulence energy dissipation rate as function of distance from the wall. The horizontal continuous line (threshold value) represents the minimum level of turbulence necessary to break the bubbles in a particular flow, while the vertical dotted line gives the location of the bubble centre when its distance from the wall is equal to the bubble radius. Values are first given for the $Re_\tau = 150$ flow with a bubble size of $220 \mu\text{m}$. This analysis confirms that the turbulence energy in the flow is much lower than that of the threshold level for bubble breakup, and it is clearly insufficient to deform the bubble structure. The maximum turbulence kinetic dissipation rate is clearly many orders of magnitude less than that required to break a bubble into two daughter bubbles of equal size. This is clearly not the case for the refrigerant R134a flow at $Re_\tau = 1154$. Here, the maximum turbulence energy dissipation rate is clearly orders of magnitude higher than that required for bubble breakup, and as a consequence a significant number of breakup events was recorded in this flow.

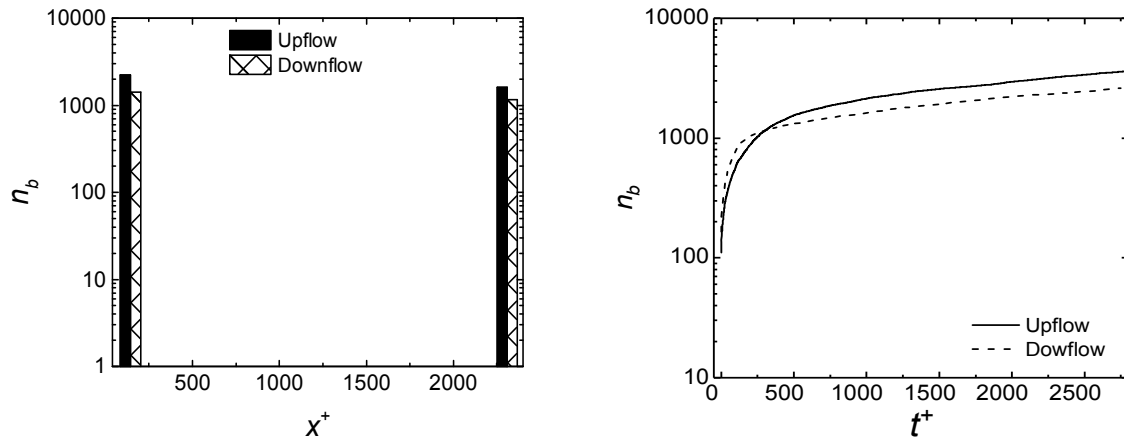


Figure 6: Number of bubble breakup events across vertical channel at $t^+ = 2000$ (left) and number of bubble coalescences with time (right) for $Re_\tau = 1154$ refrigerant case.

Results for the refrigerant flow are shown in Figs. 6 and 7, with the latter giving the number of collisions, coalescences and breakup events. Figure 6 shows the breakup distribution within the channel for the upflow and downflow cases at $t^+ = 2000$. Breakup is detected only in the near-wall regions, these being the only regions where the turbulence is high enough to promote bubble breakup. Breakup in upflow is higher than in downflow because of the larger number of bubbles that are found in the near-wall regions for the former case. Figure 6 also shows the total number of coalescences with time. These results confirm that the greater number of breakup events is recorded in upflow although, similarly to the results for the air-water flow at $Re_\tau = 2000$, the difference between the two flow directions is much less than for the lowest Reynolds number considered (Fig. 3 for the air-water flow at $Re_\tau = 150$).

Lastly, Fig. 7 presents the distribution of collisions, coalescences and breakup events across the channel for both upflow and downflow cases. As previously noted, all events occur at their highest levels in the near-wall regions. In these regions, due to the high turbulence levels, not all collisions resulted in coalescence because the contact time between bubbles was insufficient to allow for the liquid film trapped between the colliding bubbles to drain. In the centre of the channel, where the turbulence is lower and the contact time higher, almost all collisions resulted in coalescence. It is also worth noting that, where the turbulence is high enough for breakup to occur, the number of breakup events almost matches the number of coalescences, although in this flow the high turbulence encourages slightly more coalescences than breakup events.

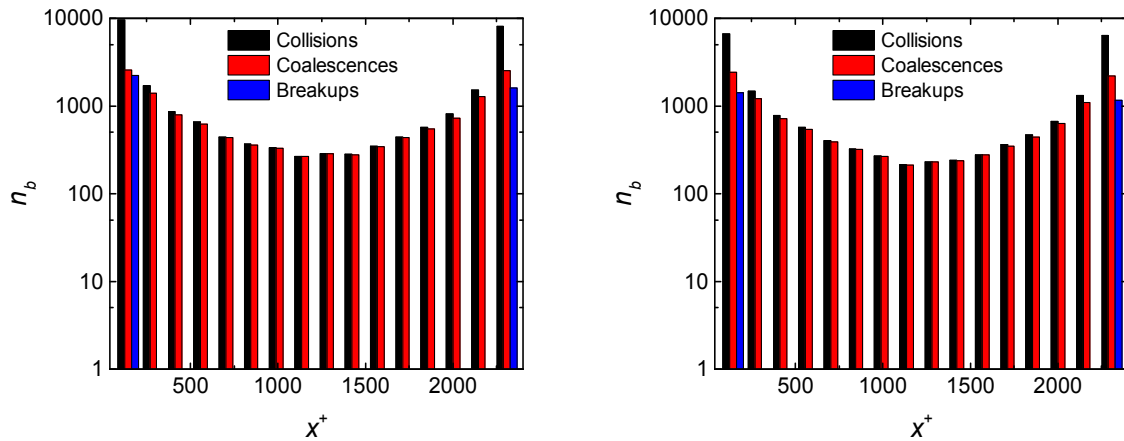


Figure 7: Number of bubble collisions, coalescences and breakup events across vertical channel in upflow (left) and downflow (right) for $Re_\tau = 1154$ refrigerant case.

4. Conclusions

Turbulent flows containing microbubbles of 220 μm diameter in a vertical channel were simulated using large eddy simulation coupled with a Lagrangian bubble tracking routine. Four-way coupled simulations were undertaken, accounting for bubble-bubble collisions, coalescences and breakup. Results were obtained for air bubbles in water at shear Reynolds numbers $Re_\tau = 150$ and 2000, and for the flow of R134a microbubbles in a refrigerant fluid flow at $Re_\tau = 1154$.

The results demonstrate that bubble-bubble interactions are greatest in the regions of high turbulence near the walls. Collisions and coalescence events are also more prevalent for upflow as a consequence of the action of the lift force that promotes bubble migration towards the highly turbulent regions near the walls. In contrast, in downflow, the lift force pushes the bubbles towards the bulk of the flow where the number of coalescences is reduced. At higher Reynolds number, the coalescence efficiency is reduced and an increased number of collisions do not result in bubble coalescence. This, and the less pronounced segregation of bubbles, causes a reduced difference in the number of coalescence events between the upflow and downflow cases.

Due to the high surface tension of the air-water mixture, bubble breakup was not observed in the water flows that were entirely coalescence dominated. Therefore, additional simulations for R134a refrigerant bubbles were performed. Results showed that breakup took place in the regions where the turbulence kinetic energy dissipation rates were high enough to deform the 220 μm bubbles injected into the high Reynolds number flow. Results also show that, once turbulence levels are high enough to overcome the surface tension stabilizing effect, breakup is favoured to approximately the same level as coalescences in the highly turbulent regions. Overall, the results demonstrate the capabilities of the model to predict microbubble behaviour and changes in the bubble size distribution due to coalescence and breakup. Future developments will include application of the methodology to flows of industrial interest and prediction of different bubble sizes and the full-evolution of the bubble size distribution.

Acknowledgements

KSA gratefully acknowledges the financial support of the Niger Delta Development Commission in Nigeria, and the opportunities that funding has given him.

References

1. B. Vreman, B.J. Geurts, N.G. Deen, J.A.M. Kuipers and J.G.M. Kuerten. Two- and four-way coupled Euler–Lagrangian large-eddy simulation of turbulent particle-laden channel flow. *Flow Turbul. Combust.*, 82: 47-71, 2009.
2. Y. Yamamoto, M. Potthoff, T. Tanaka, T. Kajishima and Y. Tsuji. Large-eddy simulation of turbulent gas-particle flow in a vertical channel: Effect of considering inter-particle collisions. *J. Fluid Mech.*, 442: 303-334, 2001.
3. S. Balachandar and J.K. Eaton. Turbulent dispersed multiphase flow. *Annu. Rev. Fluid Mech.*, 42: 111-133, 2010.
4. N. Almohammed and M. Breuer. Modeling and simulation of agglomeration in turbulent particle-laden flows: A comparison between energy-based and momentum-based agglomeration models. *Powder Technol.*, 294: 373-402, 2016.
5. D.O. Njobuenwu and M. Fairweather. Simulation of deterministic energy-balance particle agglomeration in turbulent liquid-solid flows. *Phys. Fluids*, 29: 083301, 2017.
6. E. Shams, J. Finn and S.V. Apte. A numerical scheme for Eulerian-Lagrangian simulation of bubbly flows in complex systems. *Int. J. Numer. Methods Fluids*, 67:1865-1898, 2010.
7. M. Rafique, P. Chen and M.P. Duduković. Computational modeling of gas-liquid flow in bubble columns. *Rev. Chem. Eng.*, 20: 225-375, 2011.
8. F. Hoppe and M. Breuer. A deterministic and viable coalescence model for Euler-Lagrange simulations of turbulent microbubble-laden flows. *Int. J. Multiphase Flow*, 99: 213-230, 2018.
9. L. Deju, S.C.P. Cheung, G.H. Yeoh and J.Y. Tu. Capturing coalescence and break-up processes in vertical gas-liquid flows: Assessment of population balance methods. *Applied Math. Model.*, 37: 8557-8577, 2013.
10. J.C. Lasheras, C. Eastwood, C. Martínez-Bazán and J.L. Montanes. A review of statistical models for the break-up of an immiscible fluid immersed into a fully developed turbulent flow. *Int. J. Multiphase Flow*, 28: 247-278, 2002.
11. S. Falzone, A. Buffo, M. Vanni and D.L. Marchisio. Simulation of turbulent coalescence and breakage of bubbles and droplets in the presence of surfactants, salts, and contaminants. In *Bridging Scales in Modelling and Simulation of Non-Reacting and Reacting Flows. Part I, Volume 52 (Edited by A. Parente and J. De Wilde)*, pp. 125-188, Academic Press, 2018.
12. D. Li, Z. Gao, A. Buffo, W. Podgorska and D.L. Marchisio. Droplet breakage and coalescence in liquid–liquid dispersions: Comparison of different kernels with EQMOM and QMOM. *AIChE J.*, 63: 2293-2311, 2017.
13. K.S. Asiagbe, M. Fairweather, D.O. Njobuenwu and M. Colombo. Large eddy simulation of microbubble transport in vertical channel flows. In *Computer-Aided Chemical Engineering, 40 (Edited by A. Espuña, M. Graells and L. Puigjaner)*, pp. 79-84, Elsevier, 2017.
14. M. Pang, J. Wei and B. Yu. Turbulence modulation by small bubbles in the vertical upward channel flow. *Adv. Mech. Eng.*, 5: 379839, 2013.

15. M. Pang, J. Wei and B. Yu. Study on liquid turbulence modulation by microbubbles in different turbulence layers. *Adv. Mech. Eng.*, 6: 647-467, 2014.
17. M.J. Prince and H.W. Blanch. Bubble coalescence and break-up in air-sparged bubble columns. *AIChE J.*, 36: 1485-1499, 1990.
18. C. Martinez-Bazan, J.L. Montanes and J.C. Lasheras. On the breakup of an air bubble injected into a fully developed turbulent flow. Part 1. Breakup frequency. *J. Fluid Mech.*, 401: 157-182, 1999.
19. D.G. Fox and D.K. Lilly. Numerical simulation of turbulent flows. *Rev. Geophys.*, 10: 51-72, 1972.
20. M. Germano, U. Piomelli, P. Moin and W. Cabot. Turbulence: The filtering approach. *J. Fluid Mech.*, 238: 325-336, 1991.
21. U. Piomelli and J. Liu. Large-eddy-simulation of rotating channel flow using a localized dynamic model. *Phys. Fluids*, 7: 839-848, 1995.
22. L. Di Mare and W.P. Jones. LES of turbulent flow past a swept fence. *Int. J. Heat Fluid Flow*, 24: 606-615, 2003.
23. M. Germano, U. Piomelli, P. Moin and W. Cabot. A dynamic subgrid scale eddy viscosity model. *Phys. Fluids A3*: 1760-1765, 1991.
24. F. Porté-Agel, C. Meneveau and M.B. Parlange. A scale-dependent dynamic model for large-eddy simulation: Application to a neutral atmospheric boundary layer. *J. Fluid Mech.*, 415: 261-284, 2000.
25. D.K. Lilly. The representation of small scale turbulence in numerical simulation experiments. In *Proceedings of IBM Scientific Computing Symposium on Environmental Sciences (Edited by H.H. Goldstine)*, pp. 195-210, Yorktown Heights, 1967.
26. M.R. Maxey and J.J. Riley, Equation of motion for a small rigid sphere in a nonuniform flow. *Phys. Fluids*, 26: 883-889, 1983.
27. M. Bini and W.P. Jones. Particle acceleration in turbulent flows: A class of nonlinear stochastic models for intermittency. *Phys. Fluids*, 19: 35104, 2007.
28. D. Molin, C. Marchioli and A. Soldati. Turbulence modulation and microbubble dynamics in vertical channel flow. *Int. J. Multiphase Flow*, 42: 80-95, 2012.
29. L. Schiller and Z. Naumann. A drag coefficient correlation. *Ver. Deutsch. Ing.*, 77: 318-320, 1935.
30. D. Legendre and J. Magnaudet. A note on the lift force on a spherical bubble or drop in a low-Reynolds-number shear flow. *Phys. Fluids*, 9: 3572-3574, 1997.
31. M. Breuer and M. Alletto. Efficient simulation of particle-laden turbulent flows with high mass loadings using LES. *Int. J. Heat Fluid Flow*, 35: 2-12, 2012.
32. J.N. Israelachvili. Strong intermolecular forces: Covalent and Coulomb Interactions. In *Intermolecular and Surface Forces*, pp. 53-70, Academic Press, 2011.
33. P.C. Sandip and S.D. Mahajan. A review of an alternative to R134a refrigerant in domestic refrigerator. *Int. J. Emerging Technol. Adv. Eng.*, 3: 550-556, 2013.
34. T.H.v.d. Berg, S. Luther and D. Lohse. Energy spectra in microbubbly turbulence. *Phys. Fluids*, 18: 038103, 2006.